Transient electron excitation and nonthermal electron-phonon coupling in dielectrics irradiated by ultrashort laser pulses

Nils Brouwer* and Baerbel Rethfeld
Department of Physics and OPTIMAS Research Center, Technical University of Kaiserslautern, Erwin-Schrödinger-Str. 46, 67663 Kaiserslautern, Germany
(Received 8 February 2017; revised manuscript received 31 March 2017; published 30 June 2017)

We calculate nonequilibrium electron distributions created by the absorption of an intense, ultrashort laser pulse in a transparent model-dielectric using a Boltzmann-type collision approach. We compare electron energy and particle density, as well as electron-phonon energy transfer of a full nonequilibrium simulation with values of a simulation enforcing instant thermalization, testing the inherent assumption of temperature-based models. Finally, we calculate electron-phonon coupling parameters of nonequilibrium distributions and compare these with those of thermalized distributions of the same particle and energy density. We find that the strength as well as the relaxation of the electron-phonon coupling depends considerably on the excitation parameters.

DOI: 10.1103/PhysRevB.95.245139

I. INTRODUCTION

Femtosecond laser pulses have become a standard tool of basic fundamental research. Time-resolved experiments improve our understanding of dynamical processes on the intrinsic time scales of quasiparticles in matter [1–5]. Also, their characteristic length scales have become accessible since direct lattice movement and loss of structural order have been observed with help of ultrafast x-ray diffraction techniques [6–9].

With the ever-increasing availability of intense, tabletop, femtosecond laser sources, also numerous applications have become possible, reaching from processing of biological materials and laser surgery to nanoscale material modifications and the creation of new states of matter [10–18].

Nonlinear processes enable the generation of free electrons and thus also the absorption of laser energy in actually transparent materials. The understanding of the interaction of laser light with dielectrics is not only interesting from a fundamental point of view but also important for avoiding damage to expensive optical components. Laser-induced damage of such transparent solids is usually assumed to occur when a certain density of electrons is present in the conduction band [19–21]. In that case, the optical parameters of the material change in such a way that the absorption occurs in a way similar to that in metals, and energy leading to material modification can be quickly accumulated.

In transparent dielectrics, electrons are first excited from the valence band to the conduction band by strong-field ionization, i.e., multiphoton absorption or tunnelionization [22]. Then, these newly excited electrons gain more energy by single-photon absorption. After reaching a critical energy, they can perform impact ionization, thereby exciting additional electrons to the conduction band. In Auger-like processes, an electron of the conduction band recombines with a hole in the valence band, transferring the excess energy to a conduction band electron. Auger recombination is the inverse process to impact ionization and thus counteracts the latter.

While the relevance of these basic mechanisms have been known for several decades [23–25], there are contradictory results on the relative importance of either strong-field ionization or impact ionization [20,21,26–28]. Part of the controversy has been solved with help of energy-resolved descriptions like the multiple rate equation [29–31] or kinetic models based on Boltzmann collision terms [32,33]. Particularly on ultrashort time scales, the dependence of the probability of impact ionization on the kinetic energy of the initiating electron has appeared to be crucial. This in turn strongly influences the calculated evolution of the free electron density in comparison to energy-averaged descriptions.

Recent studies have shown that rather the total absorbed energy than the density of excited electrons determines the damage threshold of dielectrics [28]. Though very high densities may lead to band structure modifications, in semiconductors accompanied with nonthermal melting processes [34], thermal heating and structural changes of the lattice can only be reached if the energy absorption in the material suffices to melt the crystal. The evolution of the temperature of the excited free carriers as well as of the phonon temperature and the carrier density has been established in the framework of a two-temperature model for the description of semiconductors [35,36]. They are also be applied for the case of dielectrics [16,37]. Such temperature-based approaches depend on integrated quantities like electron density and internal energy. Their dependence on particular electron distributions is neglected. A possible nonequilibrium distribution may, however, play a considerable role for the energy absorption of the electrons as well as for the energy transfer to the phonons.

In this work, we study the influence of the laser-induced electronic nonequilibrium on the evolution of particle density, energy density, and the energy transfer from excited electrons to initially cold phonons. To that end, we apply complete Boltzmann collision integrals in order to track the nonequilibrium distribution function of the excited electrons in the conduction band, as well as of the valence band electrons and the phonons. We show that nonequilibrium dynamics play an important role in laser-excited dielectrics, even up to the picosecond regime. For comparison, we perform simulations enforcing instant thermalization. We will show that this leads to drastic changes in the evolution of the integrated quantities, i.e., particle and energy density of the excited electrons, and in the rate at which energy is transferred from electrons to phonons.

The energy transfer rate between electrons and phonons is commonly described in relation to the temperature difference

*brouwer@physik.uni-kl.de

of both subsystems and an electron-phonon coupling parameter [35,38–41]. However, from studies of metals, it is known that nonthermalized electron systems couple differently to the lattice than thermalized electron systems [42,43]. Since the electron-phonon coupling parameter is important for all temperature-based models of ultrafast laser excitation of solids, we compare in this work the electron-phonon coupling strength obtained with our full nonequilibrium Boltzmann collision model for dielectrics with the coupling strength of corresponding thermalized distributions of the same integrated quantities. Both differ significantly during and after laser irradiation. We estimate the equilibration of these values in dependence on excitation parameters.

The paper is organized as follows: In the next section, we briefly introduce the theory and assumptions of our Boltzmann collision model. Section III is devoted to the results of our calculations. For a certain set of laser parameters, we present in Sec. III A the details of the dynamics of the distribution function of both electron bands during and after irradiation. We show the evolution of the total free electron density and energy density of the full nonequilibrium simulation as well as of the model enforcing instant thermalization. In Sec. III B we study in detail the electron-phonon energy transfer, distinguishing also between the considered electron bands and phonon modes, respectively. In Sec. III C we focus on the electron-phonon coupling parameter. We determine this parameter for four different laser pulses, having different intensities and pulse duration, but all the same fluence. We compare these values at time instants during as well as after irradiation, with values obtained for Fermi-distributed electrons and Bose-distributed phonons. We close the work with a short summary and conclusions.

II. THEORY

To investigate the electron-phonon coupling under nonequilibrium conditions, e.g., in laser-excited dielectrics on the femtosecond timescale, it is necessary to calculate the transient distribution functions of electrons and phonons. To achieve this, we used a homogeneous, isotropic approximation of the Boltzmann equation, further extending the Boltzmann collision model presented in Refs. [32,44,45]. The conduction band is modeled with a quasi-free-electron dispersion relation with an effective mass as introduced in Ref. [32]. The laser absorption is modeled with transient reflectivity and a dielectric function as presented in Ref. [44]. In addition, we include the full valence band dynamics, modeling the valence band with its own effective mass and implement a transient screening length, based on the distribution function of conduction and valence band electrons and Auger recombination as inverse process to impact ionization [45]. Moreover, we now include the possibility of energy exchange between both electronic bands without particle transfer, better known as electron-hole scattering.

In total, we have now two equations for the electron distribution functions f_ν:

$$\frac{df_\nu}{dt} = \sum_{\text{coll}} \left.\frac{\partial f_\nu}{\partial t}\right|_{\text{coll}} = \left.\frac{\partial f_\nu}{\partial t}\right|_{\text{multiph}} + \left.\frac{\partial f_\nu}{\partial t}\right|_{\text{imp. ion.}} + \left.\frac{\partial f_\nu}{\partial t}\right|_{\text{Auger}} + \left.\frac{\partial f_\nu}{\partial t}\right|_{e\text{-}e} + \left.\frac{\partial f_\nu}{\partial t}\right|_{e\text{-}h} + \left.\frac{\partial f_\nu}{\partial t}\right|_{e\text{-}ph} + \left.\frac{\partial f_\nu}{\partial t}\right|_{e\text{-}ph\text{-}pt}, \quad (1)$$

where ν is the band index, that is, either conduction band (cb) or valence band (vb). $\left.\frac{\partial f_\nu}{\partial t}\right|_{\text{coll}}$ represent the included collisions, each given by a complete Boltzmann collision integral. We include strong field ionization [22] (multiph), impact ionization (imp. ion), Auger recombination (Auger), electron-electron intraband collisions (e-e), electron-hole collisions (e-h), electron-phonon collisions (e-ph), and electron-phonon-photon (e-ph-pt) collisions.

The conduction band versions of the collision integrals (for multiph, imp. ion, e-e, e-ph, and e-ph-pt) have already been described in Refs. [32] and [44]. All collision integrals are based on first-order perturbation theory using Fermi's golden rule. The resulting summation over those states taking part in a collision were approximated as integrals and further simplified by assuming isotropy. For further details, please consult Refs. [32] and [44], as well as references therein. The valence band terms can be derived analogously to the conduction band terms and only differ due to the different dispersion relations, i.e., in our case the different effective masses. The term for Auger recombination, which enables a balance with its inverse process, impact ionization, was presented in Ref. [45]. Finally, we included electron-hole collisions, which exchange energy between both bands.

In addition to the two electron bands, we also model three phonon modes, that is one longitudinal acoustic (LA) and two longitudinal optical modes (LO1 and LO2). We neglect transversal modes, umklapp- and phonon-phonon processes. The set of equations for the distribution functions s_β of the three considered phonon modes reads

$$\frac{ds_\beta}{dt} = \sum_{\text{coll}} \left.\frac{\partial s_\beta}{\partial t}\right|_{\text{coll}} = \left.\frac{\partial s_\beta}{\partial t}\right|_{ph\text{-}e} + \left.\frac{\partial s_\beta}{\partial t}\right|_{ph\text{-}e\text{-}pt}, \quad (2)$$

where β is the mode index. $\left.\frac{\partial s_\beta}{\partial t}\right|_{\text{coll}}$ represent the included collision integrals: Phonon-electron collisions (ph-e) represent the change of the phonon distributions due to collisions with conduction band electrons as well as valence band electrons, while phonon-electron-photon collisions (ph-e-pt) represent the change of the phonon distribution due to intraband photon absorption by conduction band electrons as well as valence band electrons.

Since electron-phonon energy transfer is the focus of this work, we will now take a closer look at the contributing collision integrals. For the electron distribution functions, the collision term for e-ph and e-ph-pt collisions is given by

$$\left.\frac{\partial f_\nu(\varepsilon)}{\partial t}\right|_{e\text{-}ph\text{-}pt} = \frac{1}{2\pi\hbar^3}\frac{m_\nu^*}{k_\nu(\varepsilon)}\sum_\beta\sum_{l=-\infty}^{\infty}\left\{\int_{q\in Q^+_{\beta,l,\nu}} dqq|M_{e\text{-}ph}(q,\beta)|^2\bar{J}_l^2(q,E_L,\omega_L)f_\nu(\varepsilon_+)[1-f_\nu(\varepsilon)]\right.$$
$$\times\,[s_\beta(q)+1] - f_\nu(\varepsilon)[1-f_\nu(\varepsilon_+)]s_\beta(q)$$
$$\left.+\int_{q\in Q^-_{\beta,l,\nu}} dqq|M_{e\text{-}ph}(q,\beta)|^2\bar{J}_l^2(q,E_L,\omega_L)f_\nu(\varepsilon_-)[1-f_\nu(\varepsilon)]s_\beta(q) - f_\nu(\varepsilon)[1-f_\nu(\varepsilon_-)][s_\beta(q)+1]\right\}, \quad (3)$$

where m_v^* is the effective mass and k_v is the electron wave number in band v. The number of absorbed phonons is given by l and $l = 0$ therefore refers to plain e-ph collisions. q is the phonon wave number and the electron-phonon matrix element is denoted by $M_{e\text{-}ph}(q,\beta)$. The laser field amplitude inside the material, E_L, is calculated from the external laser intensity [44], ω_L is the laser frequency, and $\bar{J}_l^2$ is the direction-averaged squared Bessel function of order l. The electron energy state is given by ε with $\varepsilon_\pm = \varepsilon + l\hbar\omega_L \pm \hbar\omega_\beta(q)$, where $\hbar\omega_\beta(q)$ is the phonon energy of mode β. Momentum conservation is ensured by the integration interval $Q^\pm_{\beta,l,v}$. The electron-phonon matrix element is denoted by $M_{e\text{-}ph}(q,\beta)$.

For the phonon distribution functions, the corresponding collision term reads

$$\left(\frac{\partial s_\beta(q)}{\partial t}\right)_{ph\text{-}e\text{-}pt} = \frac{1}{2\pi\hbar^5}\frac{m_v^{*2}}{q}\sum_v\sum_{l=-\infty}^{\infty}|M_{e\text{-}ph}(q,\beta)|^2\bar{J}_l^2(q,E_L,\omega_L)$$
$$\times\frac{1}{2}\Bigg\{\int_{\varepsilon\in K^+_{\beta,l,v}} d\varepsilon f_v(\varepsilon_+)[1-f_v(\varepsilon)][s_\beta(q)+1] - f_v(\varepsilon)[1-f_v(\varepsilon_+)]s_\beta(q)$$
$$+\int_{\varepsilon\in K^-_{\beta,l,v}} d\varepsilon f_v(\varepsilon)[1-f_v(\varepsilon_-)][s_\beta(q)+1] - f_v(\varepsilon_-)[1-f_v(\varepsilon)]s_\beta(q)\Bigg\}, \quad (4)$$

where $K^\pm_{\beta,l,v}$ is the integration interval for the electron energy ensuring momentum conservation.

For acoustic phonons, we use a deformation potential theory approximation leading to the matrix element [32,45]

$$|M_{e\text{-}ph}(q,\beta)|^2 = \frac{\hbar C_\beta^2 q^2}{2\rho\omega_\beta(q)[1+(q_0/q)^2]}, \quad (5)$$

where C_β is the deformation potential of mode β, q_0 is the inverse screening length, and ρ is the mass density of the material.

For polar optical phonons [32,45], we apply

$$|M_{e\text{-}ph}(q,\beta)|^2 = \frac{e^2}{\varepsilon_0}\frac{\hbar\omega_\beta}{2[1+(q_0/q)^2]}\left(\frac{1}{\varepsilon_\infty}-\frac{1}{\varepsilon_r}\right), \quad (6)$$

where e is the elemental charge, ε_0 is the vacuum permittivity, ε_r is the relative permittivity, and ε_∞ is the optical permittivity. q_0 is the inverse screening length, which is calculated transiently [45] from electron distribution functions of both bands. Note that the Boltzmann equation is inherently using the Markov approximation and therefore neglecting memory effects, and correlation effects are only considered in form of the aforementioned transiently calculated static screening.

In total, we obtain a system of five coupled integrodifferential equations that has to be solved numerically. We discretized the energy axis for the electron bands and the wave number axis for the phonon modes. To gain an accurate measure of the electron-phonon energy transfer, minimizing interpolation errors is very important. Since the typical electron energy scale in a laser excited dielectric is on the order of the band-gap energy and therefore several orders of magnitudes higher than a typical phonon energy, we chose to discretize the electron energy in very tiny steps, 3000 points for each band, while we used only 75 points for each phonon mode. In order to keep computational cost manageable, we use the GNU scientific library implementation [46], of the MISER Monte Carlo integration algorithm, to calculate the various electron-electron integrals. Finally, the system of differential equations was solved using an adaptive time step, between 1 as and 1 fs, based on the change of the distribution function.

III. RESULTS

In this section, we present results of our simulation based on the Boltzmann collision model for a model-dielectric based on material parameters of fused silica. We use the same values as presented in Ref. [45] and references therein, with the exception that the parameters for the polar electron-phonon matrix element were taken from Ref. [47]. Here, we shortly summarize the most important parameters: sound velocity of longitudinal acoustic (LA) phonon mode [32] $v_s = 5935\,\mathrm{m/s}$ entering the dispersion relation, $\omega(q) = v_s q$; deformation potential of the LA mode [48] $C_\beta = 6\,\mathrm{eV}$ entering Eq. (5); phonon energies and polar matrix element [47] of the first longitudinal optical mode (1 LO) $\hbar\omega = 0.063\,\mathrm{eV}$, $\varepsilon_\infty^{-1} - \varepsilon_r^{-1} = 0.063$, and second longitudinal optical mode (2 LO) $\hbar\omega = 0.153\,\mathrm{eV}$, $\varepsilon_\infty^{-1} - \varepsilon_r^{-1} = 0.143$ entering Eq. (6); and effective mass in valence band [45] $m_v^* = 3.52 m_e$ and conduction band [48] $m_c^* = m_e$.

With these parameters, the model is suitable for intensities between 10^{17} and $10^{19}\,\mathrm{W/m^2}$, since lower intensities will not lead to sufficient excitation and at higher intensities relativistic effects would have to be taken into account. The pulse duration should not be much smaller than 50 fs, as that would stretch the limits of the carrier envelope approximation, for visible laser wavelength.

A. Nonequilibrium electron dynamics

In this section, we analyze the nonequilibrium electron distribution, density, and energy in a dielectric exited by an intense ultrashort laser pulse and compare with a modified simulation enforcing instant thermalization. The system is assumed to be excited with a 400-nm, $\tau_\mathrm{L} = 100\,\mathrm{fs}$ FWHM Gaussian-shaped laser pulse centered at 0 fs with a maximum intensity of $I_\mathrm{max} = 2\times10^{18}\,\mathrm{W/m^2}$.

Figure 1 shows the electron distribution, resolved by electron energy, at different times during excitation, namely on the rising flank (black solid line), the maximum (red dotted line), and the falling flank of the pulse (green dashed line). Here in Figs. 1 and 2 the transient distributions of conduction

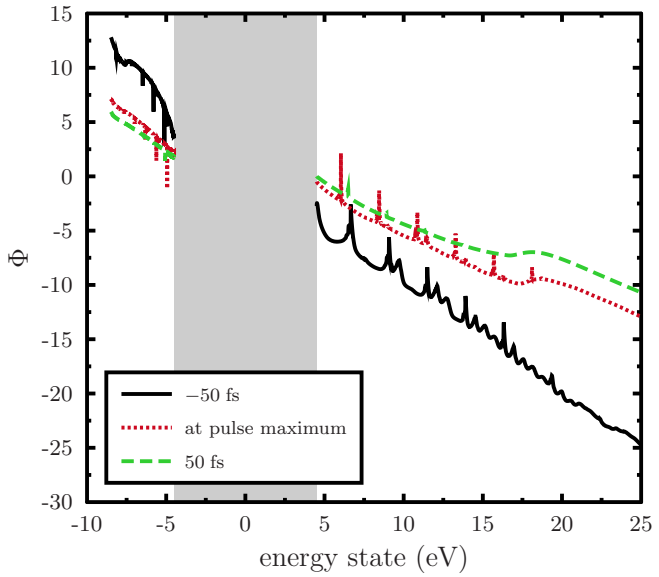

FIG. 1. Quasilogarithmic representation (7) of the nonequilibrium distribution of valence and conduction band electrons at different times during laser pulse of $\tau_L = 100$ fs (FWHM).

and valence band electrons during and after laser excitation are shown in a pseudologarithmic representation,

$$\Phi = -\ln\left(\frac{1}{f} - 1\right). \tag{7}$$

Similar to a logarithmic representation, it shows variations in the distribution on different orders of magnitude, while still being a monotonously rising function of the electron distribution. Moreover, it directly resolves also the distribution of holes as distribution of valence band electrons. In addition, Fermi distributions are represented by straight lines with slopes inversely proportional to the temperature of the Fermi distribution.

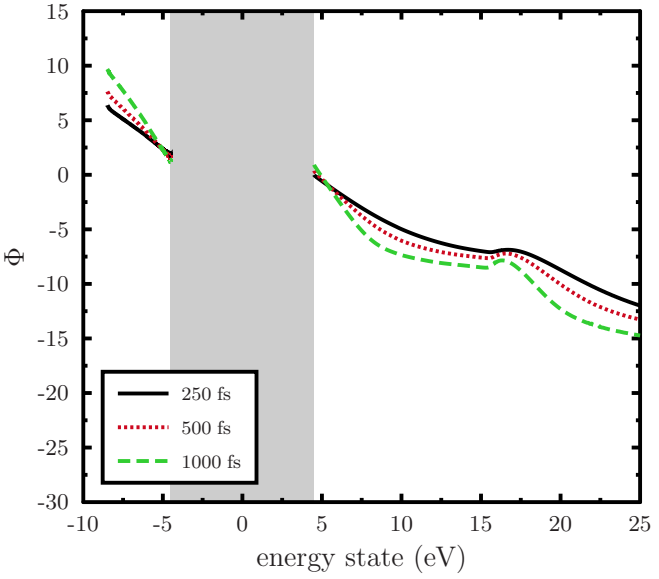

FIG. 2. Quasilogarithmic representation (7) of the nonequilibrium distribution of valence and conduction band electrons after laser pulse. The time after pulse maximum is indicated.

The black solid line in Fig. 1 shows the distribution at 50 fs before maximum laser intensity, when half of $I_{\max}$ is reached. Its most prominent feature is the peak structure in the conduction band and the corresponding dip structure in the valence band. These arise from a combination of several effects: First, we have multiphoton ionization of the lowest possible order. For the combination of photon energy and band gap used in the present calculation, the process is of third order. In addition, higher order multiphoton ionization, called above-threshold ionization (ati), contributes to the peak structure. With equal effective masses in conduction and valence bands, momentum conservation would lead to ati peaks half a photon energy above the lower order peak. In our calculations, the peaks are shifted by less than half the photon energy as compared to the peak of lower order, due to different effective masses in valence and conduction band. Finally, intraband single-photon absorption will reproduce each peak at an energy larger by one photon energy, leading to an ever-increasing number of increasingly smaller peaks at higher electron energies. A more detailed description of the peak structure can be found in Ref. [45].

The red dotted curve in Fig. 1 shows the electron distribution at maximum laser intensity. In comparison to the black solid line, it features similar peaks and dips, but their location has shifted towards the band gap. This shift in the energy of the peak positions results from the increase in laser field strength raising the effective ionization potential [22,32,45]. As a result, the third-order multiphoton peak has completely vanished. The lowest order mpi is now a fourth-order process. In addition, the distribution function of conduction band electrons has increased, while the distribution function of valence band electrons has decreased. This is expected as electrons are excited from the valence band to the conduction band.

Finally, conduction band states over about 18 eV are slightly more populated than the overall slope of the distribution would suggest. This is the result of Auger recombination processes already contributing to the population of higher energy conduction band states, resulting in a so-called Auger bump [49].

The green dashed curve in Fig. 1 shows the electron distribution function at 50 fs after maximum laser intensity. In comparison to the red dotted curve, the distribution function of conduction band electrons has further increased, while the distribution function of valence band electrons has further decreased. However, the peak and dip structures are nearly completely washed out. This can be attributed to the increased effect of electron-electron collisions leading to thermalization and the decreasing strength of strong field ionization. The remaining visible peak and dip have moved away from the band gap again, in accordance with the decreasing laser field strength. Finally, the Auger bump has grown further.

In Fig. 2, the conduction and valence band distribution functions are shown for times well after the laser pulse. Again, the pseudologarithmic representation (7) was chosen. The black solid curve shows the distribution functions 250 fs after the laser pulse maximum. In contrast to Fig. 1, no sharp peaks or dips are visible. This is not surprising, since those were caused by the laser pulse, which is negligible at a time of

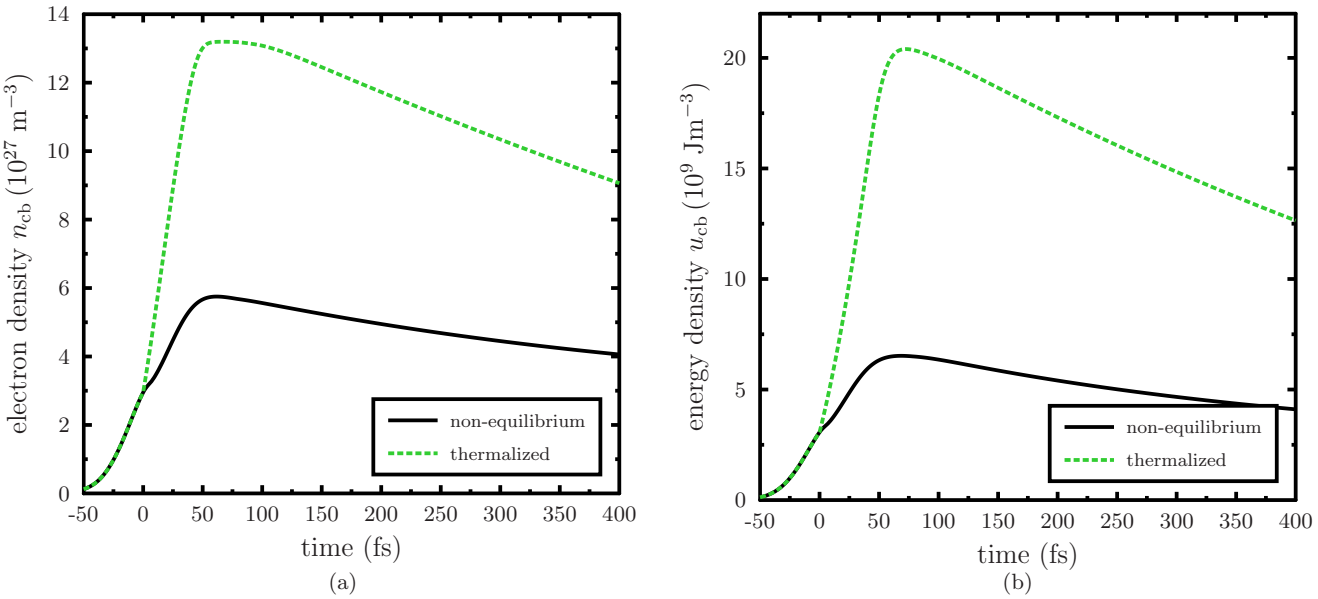

FIG. 3. (a) Conduction band electron density n_{cb} and (b) energy density u_{cb} for the full nonequilibrium simulation and the simulation enforcing instant thermalization.

2.5 FWHM after the maximum laser intensity. However, the Auger bump is still present.

The red dotted curve in Fig. 2 shows the distribution functions 500 fs after the laser pulse maximum. It differs from the solid black curve in two ways: Its overall slope is steeper and the Auger bump is more pronounced. The increased steepness of the curve is caused by electron-phonon collisions, which reduce the overall energy content of the electron system by removing electrons from high-energy states and adding them in low-energy states, therefore increasing the steepness of the distribution. The second feature, the growing Auger bump, is actually directly related to the first feature: Since the whole electron system has less energy per electron than before, the ratio of conduction band electrons to valence band electrons must shift in favor of valence band electrons, in order to reach an equilibrium of electron temperature and density. Auger recombination decreases conduction band density, while increasing the energy per electron in the conduction band. Such a high-energy tail of the electron distribution caused by Auger recombination has also been found in the conduction band of aluminum after excitation of electrons from deep shells with extreme ultraviolet radiation [50,51].

These two trends continue in the picosecond regime, as is visible in the green dashed curve in Fig. 2, which shows the electron distribution functions 1000 fs after the laser pulse maximum.

A steeper distribution in Φ representation would correspond to lower temperature if the system was thermalized. However, as the curves are not exactly linear even for as long as 1 ps, the system actually is still not thermalized on a picosecond timescale.

Thermalization is an asymptotic process. Therefore, full thermalization would, strictly speaking, require an infinite amount of time, yet the concept of such a temperature is widely applied even down in the subpicosecond regime. So the real question is how much of a difference do the nonequilibrium distribution functions make? To test this, we modify our simulation to enforce instant thermalization; that is, after each time step we calculate the energy density of each electronic and phononic distribution function as well as the particle density of the electronic bands. The distribution functions are then replaced by Fermi functions of the same particle and energy density or Bose functions of the same energy density, respectively, and the changes of these distributions are determined through Eqs. (1) and (2). The system is replaced by a thermalized system at each numerical time step. We start this procedure at peak laser intensity ($t = 0$ fs) and compare electron densities and energy densities with the results of the full nonequilibrium simulation.

In Fig. 3(a), the time evolution of the conduction band electron density n_c is shown. It is calculated from the conduction band distribution $f_c(\varepsilon)$ using the density of states $D(\varepsilon)$:

$$n_{cb} = \int f_{cb}(\varepsilon)\, D(\varepsilon) d\varepsilon. \tag{8}$$

The black solid curve represents the full nonequilibrium simulation. The conduction band electron density first rises until about 50 fs after maximum laser intensity, reaching nearly $n_c = 6\times10^{27}$ m^{-3}, and then slowly decreases again. Interestingly, the slope of the curve decreases slightly around maximum laser intensity. An analysis of the collision terms (not shown here) shows that this can be attributed to Pauli blocking in the final levels of multiphoton ionization in the conduction band.

The green dotted curve in Fig. 3(a) shows the evolution of the conduction band electron density for the simulation enforcing instant thermalization. In contrast to the black solid curve, it rises much faster and higher, reaching about $n_{cb} = 13\times10^{27}$ m^{-3}, and then also decreases at a faster rate.

In contrast to the nonequilibrium simulation, there is no visible decrease in the slope around maximum laser intensity. This can be explained by the instantaneous depletion of the final levels of multiphoton ionization down to an equilibrium occupation through instant thermalization, thereby avoiding Paul blocking.

Figure 3(b) shows the time evolution of the conduction band electron energy density u_{cb}. It is calculated from the conduction band distribution:

$$u_{\mathrm{cb}} = \int f_{\mathrm{cb}}(\varepsilon)\,\mathrm{D}(\varepsilon)\varepsilon d\varepsilon. \tag{9}$$

The black solid curve represents the full nonequilibrium simulation. The conduction band electron energy density u_{c} first rises until about 70 fs after maximum laser intensity, reaching more than $u_{\mathrm{c}} = 6\times10^{9}\,\mathrm{Jm}^{-3}$, and then slowly decreases again.

The green dotted curve in Fig. 3(b) shows the evolution of the conduction electron energy density u_{c} for the simulation enforcing instant thermalization. In contrast to the black solid curve, it rises much faster and higher, reaching over $u_{\mathrm{c}} = 20\times10^{9}\,\mathrm{JM}^{-3}$, and then also decreases at a faster rate.

While both particle and energy density show a similar discrepancy between both simulations, the difference is even more pronounced for the latter.

Enforcing thermalized distribution functions has several effects, including e.g. an initially lower inverse screening length; however, the main reason for the difference in electron excitation visible in Figs. 3(a) and 3(b) is enhanced multiphoton ionization. Since the final levels of multiphoton ionization are instantly restored to the values of a thermalized distribution whose Fermi edge is below those energy levels, Pauli blocking has a considerably smaller effect on the multiphoton ionization rate than in the nonequilibrium simulation. This initial enhancement of electron excitation is then further amplified by a subsequent change in optical parameters, mainly laser light absorption, due to the increased conduction band density.

In conclusion, we see a considerable difference between thermalized and nonequilibrium values of the integrated quantities of the conduction band electrons, i.e. particle and energy density. This is particularly remarkable, since, for instance, the conduction band electron density is often used as a damage criterion.

B. Electron-phonon energy transfer

In this section, we will show electron-phonon energy transfer rates resulting from our full nonequilibrium simulation and compare them to the rates of the simulation enforcing instant thermalization. We analyze the contribution of the conduction and valence band electrons as well as the contribution of the different phonon modes.

In Fig. 4, the total energy transfer rate from conduction and valence band to all considered phonon modes is shown.

The combined energy transfer rate $\frac{\partial u}{\partial t}|_{\text{e-ph}}$ is calculated from the change of both electron distribution functions due to electron-phonon collisions:

$$\left.\frac{\partial u}{\partial t}\right|_{e\text{-ph}} = \sum_{\nu}\int \left.\frac{df_{\nu}(\varepsilon)}{dt}\right|_{e\text{-ph}} \mathrm{D}(\varepsilon)\varepsilon d\varepsilon. \tag{10}$$

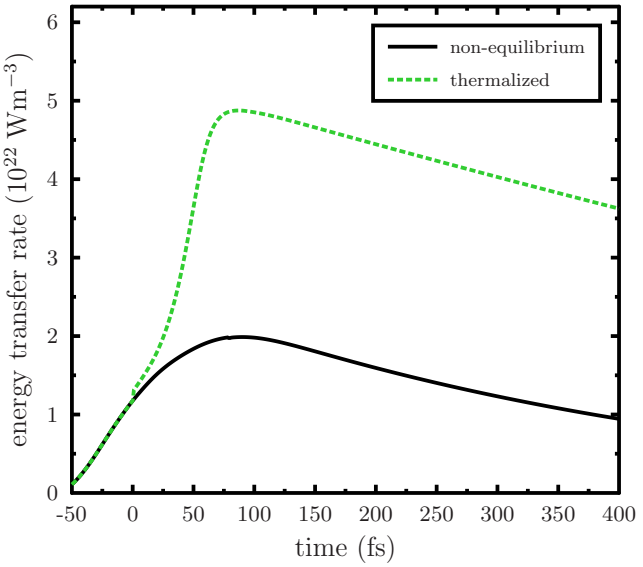

FIG. 4. Total electron phonon energy transfer rate from valence and conduction band to all considered phonon modes for the full nonequilibrium simulation and the simulation enforcing instant thermalization.

The black solid curve shows the time evolution of the energy transfer rate for the full nonequilibrium simulation, while the green dotted curve shows the same variable for the simulation enforcing instant thermalization. Both curves first increase, reaching their maximum value at about 80 fs after maximum laser intensity, and then decrease again. However, the green dashed curve increases much faster and reaches a maximum of about 2.5 times higher than the black solid curve. The decrease of the thermalized simulation is slightly steeper than that of the nonequilibrium simulation. This means, when assuming instant thermalization, more energy is transferred to the phonon system faster. Since, as we have shown in Ref. [45], electron-phonon coupling in dielectrics strongly depends on conduction band electron density, a major part of the increased energy transfer rate most likely can be attributed to the enhanced density of conduction band electron shown in Fig. 3(a). However, also the shape of the distribution itself leads to a difference between electron-phonon energy transfer in a thermalized and in a nonequilibrium system, as will be discussed in Sec. III C.

Figure 5 shows the time evolution of the energy transfer rate to the phonons, but in contrast to Fig. 4, the contribution of valence band and conduction band electrons is shown separately. The black solid curve shows the contribution of the conduction band electrons to the energy transfer rate. The red dotted curve shows the contribution of the valence band electrons to the energy transfer rate. The results of the full nonequilibrium simulation are represented by thick lines, while the results of the simulation enforcing instant thermalization are represented by thin lines.

It is clearly visible that the contribution of the valence band electrons to the electron-phonon energy transfer rate is the dominating contribution both for the full nonequilibrium and for the thermalized simulation. Since we used identical

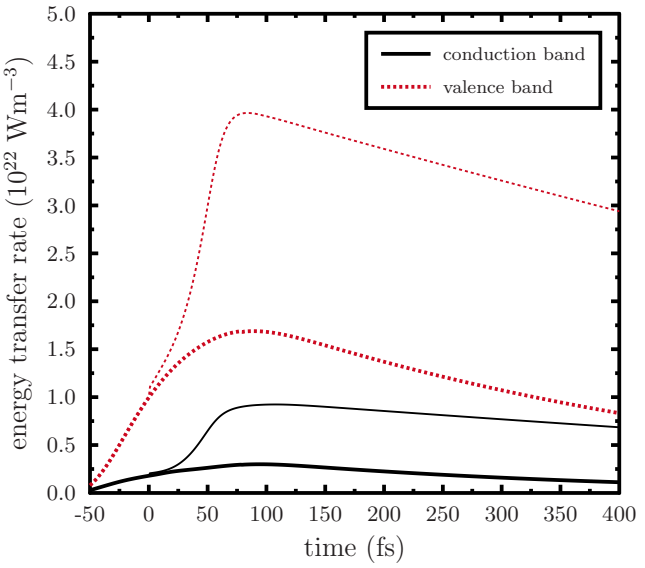

FIG. 5. The energy transfer from valence and conduction band to all considered phonon modes is shown for the case of full nonequilibrium (thick lines) and enforced instant thermalization (thin lines).

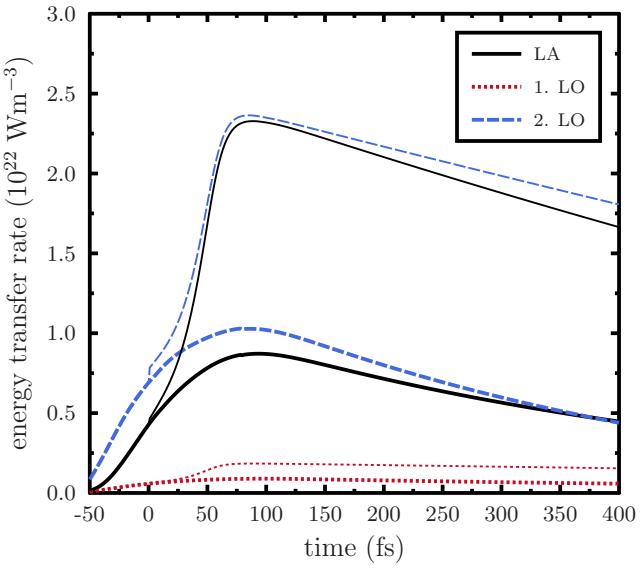

FIG. 6. Energy transfer from both bands combined to each phonon mode in the case of full nonequilibrium (thick lines) and instant thermalization (thin lines).

matrix elements for conduction and valence band electrons, this can be attributed to the higher effective mass and therefore higher density of states of the valence band. Furthermore, the conduction band electron-phonon energy transfer rates decrease more slowly than these of the valence band for both the nonequilibrium and the thermalized simulation. Note that the relative contribution of valence and conduction band electrons to the electron-phonon energy transfer might vary when introducing more realistic material parameters. However, it is still likely that the contribution of valence band electrons is much higher than one would expect in a dielectric under equilibrium conditions.

Figure 6 shows the time evolution of the electron-phonon energy transfer rate for both electron bands combined, but separated for the different phonon modes. The full nonequilibrium simulation results are represented by thick lines, while the simulation enforcing instant thermalization is represented by thin lines. The energy transfer to the longitudinal acoustic (LA) mode is represented by a solid black curve. The energy transfer to the first longitudinal optical mode (1 LO) is represented by a red dotted line. The energy transfer to the second optical mode (2 LO) is represented by a blue dashed curve. The qualitative shape of the curves is similar to their respective equivalent (i.e., their sum) in Fig. 4.

Both in the full nonequilibrium simulation as well as in the simulation enforcing instant thermalization, most energy is absorbed by the second longitudinal optical mode, but nearly as much energy is absorbed by the longitudinal acoustic mode. In contrast, the first longitudinal optical mode only plays a minor role. Hence, electron-phonon energy transfer is mode dependent. This might indicate that even if the concept of a temperature would hold, a separation of the phonon temperatures by modes might be necessary in temperature-based models. A similar idea was recently proposed for metals with regard to transversal modes [52]. Those findings, as well as ours shown in Fig. 6, raise the question of phonon thermalization as well as phonon-phonon relaxation times. It is usually assumed that phonons equilibrate on a picosecond timescale (e.g., calculations for Si in Ref. [53]).

C. Electron-phonon coupling parameter

In this section, we want to discuss the influence of nonequilibrium distribution functions on the electron-phonon coupling parameter. This parameter is applied in the framework of the two-temperature model [35,38] and connects the energy transfer rate to the temperature difference of electrons and phonons. As we have seen in the previous two sections, enforcing instant thermalization leads to an enhanced electron excitation with respect to their particle density as well as their energy density. This leads to an enhanced electron-phonon energy transfer rate across all considered bands and modes. In part, the differences can be attributed to a more effective excitation of conduction band electrons in the thermalized simulation. In practice, the parameters for laser absorption in the two-temperature model will often be obtained by fitting to experimental values. Therefore, the disparity in excitation strength might be compensated for already.

However, a possible influence of nonequilibrium distributions on electron-phonon coupling may go beyond the differences in particle and energy density. We will study such effects in the current section.

To rule out the effect of particle and energy densities, we compare the electron-phonon coupling strength after laser excitation with the electron-phonon coupling of thermalized electron distribution, determined such that they have the same particle and energy density; see Eqs. (8) and (9). The temperatures of these corresponding equilibrium distributions enter the calculation of the electron-phonon coupling parameter also in the nonequilibrium case, where a temperature

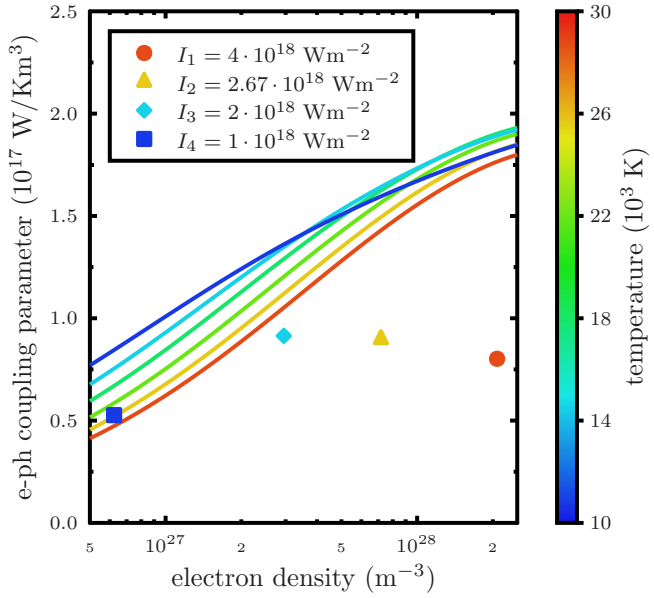

FIG. 7. The electron-phonon coupling of conduction band electrons to second longitudinal optical mode at laser peak of four different excitations with the same incident fluence is represented by geometric symbols. The applied pulse durations τ_1, τ_2, τ_3, and τ_4 have been 50, 75, 100, and 200 fs, respectively. Electron-phonon coupling parameters of equilibrium systems are shown as lines. The color code represents the corresponding electron temperature, or, in the case of the nonequilibrium situation, their quasitemperature.

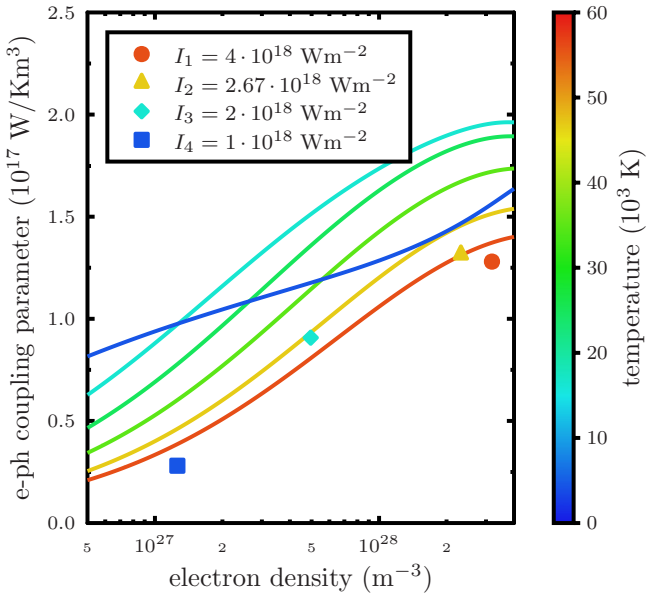

FIG. 8. Electron-phonon coupling of conduction band electrons to second longitudinal optical mode at twice laser pulse length after laser peak. For notation, see Fig. 7; however, note the different temperature color scale.

is not strictly defined. We will call the temperature of the corresponding equilibrium distribution the quasitemperature of the distribution.

As we have seen in the previous section, the electron phonon energy transfer rate between the various bands and modes differs quite significantly. Moreover, instead of one electron-phonon coupling parameter for the whole system, there is actually one electron-phonon coupling parameter for every combination of an electron band and a phonon mode. Thus, even when assigning quasitemperatures, each band and each mode will have in general a different temperature. In this work, we will focus on the electron-phonon coupling parameter for the coupling of the conduction band to the second optical phonon mode. It is calculated from the electron-phonon energy transfer rate $\partial u/\partial t$ between the conduction band and the second optical mode, the phonon (quasi)temperature $T_{\mathrm{ph,2.LO}}$ of the second longitudinal optical mode and the conduction band electron temperature or quasitemperature, respectively, $T_{\mathrm{e,cb}}$ as

$$g_{\mathrm{cb,2.LO}} = \frac{1}{T_{\mathrm{ph,2.LO}} - T_{\mathrm{e,cb}}} \left.\frac{\partial u}{\partial t}\right|_{\mathrm{e\text{-}ph(cb,2.LO)}}. \qquad (11)$$

In Figs. 7 and 8, the electron-phonon coupling parameter is shown versus the conduction band electron density. The solid lines indicate the coupling parameters calculated from equilibrium distributions of different electronic temperatures, which are indicated by color coding. Details on the general dependence of the equilibrium electron-phonon coupling parameter on the conduction band electron density and temperature can be found in our previous work [45].

We compare the coupling strengths of laser-induced nonequilibrium electron distributions with their corresponding equilibrium distributions by choosing four different laser pulses with the same incident fluence,

$$F = \int_{-\infty}^{+\infty} I_{\max} \exp\left(-\frac{(2t)^2}{\tau_L^2} \ln 2\right) \mathrm{d}t = \frac{\sqrt{\pi}}{2\sqrt{\ln 2}} I_{\max} \tau_L, \qquad (12)$$

but different pulse duration τ_L.

In Figs. 7 and 8 the electron-phonon coupling strengths, calculated by Eq. (11) at different instants of time, are shown as symbols. Figure 7 shows the transient nonequilibrium electron-phonon coupling values at the maximum of different laser pulses. The quasitemperature of the corresponding nonequilibrium distribution is indicated by color coding, while the conduction band density reached at that time is indicated on the x axis. Pulse lengths between 50 and 200 fs were chosen for the nonequilibrium calculation and the intensity was adjusted to yield the same incident fluence.

Looking at the densities and quasitemperatures of the nonequilibrium simulations, we see that the short, intense pulses lead to stronger excitations than longer, weaker pulses with the same fluence. Nevertheless, the electron-phonon couplings strength is comparable for all considered excitations. The nonequilibrium electron-phonon coupling values are, however, systematically lower than the corresponding equilibrium electron-phonon coupling parameters that match their quasitemperature and conduction band densities. The more intense, shorter pulses leading to the highest densities show the biggest deviations. Intense pulses lead to a stronger deviation of the distribution function than less intense pulses. This results in a notable increase of the inverse screening length, which is the main reason for the decreased electron-phonon coupling in the nonequilibrium simulation.

Figure 8 shows the transient nonequilibrium electron-phonon coupling values at a time instant of two pulse durations (FWHM) after the maximum intensity for different laser pulses as dots, with the quasitemperature of the corresponding distribution functions indicated by color coding. The same pulse parameters as in Fig. 7 were chosen. In contrast to the case during irradiation shown in Fig. 7, now the shorter, more intense pulses (red circle) lead to electron-phonon coupling values pretty close to those of equilibrium distributions comparable to their quasitemperature, while the coupling strengths of the weaker and longer pulses (blue square) have deviated even further away, as compared to those in Fig. 7. As is already known for metals [42], nonequilibrium distributions resulting from stronger excitations thermalize faster, and therefore the observed smaller deviation from equilibrium electron-phonon coupling values confirms this finding also for the excitation of dielectrics.

IV. SUMMARY AND CONCLUSIONS

In this work, we have studied the nonequilibrium dynamics of laser-excited electrons and phonons in a dielectric with help of complete Boltzmann collision integrals. We have calculated the nonequilibrium distributions of the conduction band and valence band electrons, respectively, and determined their density and energy as well as the energy transfer to the phonon system. Three longitudinal phonon modes have been considered.

We have discussed the laser-excited nonequilibrium distributions of the electrons and have shown that interband processes as Auger recombination can hinder thermalization for times up to the picosecond regime, as long as the electronic system loses energy. We have shown that the energy transfer rate to phonons strongly depends on the electron band as well as on the considered phonon mode.

For comparison, we have performed simulations enforcing instant thermalization in each time step and compared the results to the full nonequilibrium simulation. We have seen that the nonequilibrium distribution leads to a reduced density of excited electrons as well as a reduced energy content as compared to an instantly thermalized situation. We conclude that calculations of integrated quantities like temperature or density should be interpreted carefully. This might be particularly important for the estimation of damage thresholds, where the electron density and the absorbed energy are crucial parameters.

Finally, we have studied the electron phonon coupling strength, comparing the energy loss of electron distributions of the same respective electron density and internal energy. We have shown that the shape of the distribution function, i.e., a thermalized distribution vs a laser excited nonequilibrium distribution, plays a significant role for the strength of electron-phonon coupling. For high intensities and short pulses, the difference in the coupling strengths vanishes on a time scale shorter than 100 fs, while for the lowest considered intensity it remains up to half a picosecond. Thus, with respect to the electron-phonon coupling parameter, strong excitations thermalize faster than weaker excitations.

We conclude that the parameters of temperature-based descriptions may depend not only on the considered material but also on the particular excitation conditions. Moreover, in such models, a separation of electron bands and phonon modes is likely to be necessary, similar to the way proposed in Ref. [52] for metals for transversal and longitudinal phonon modes. Note that it was shown for the optical excitation of semiconductors, that Boltzmann collision integrals tend to underestimate the thermalization time [54,55] on the femtosecond time scale. In case this holds for strongly laser-excited dielectrics, one should be even more cautious when applying thermalized models. Further studies, e.g., using nonequilibrium Green's function methods, would be necessary to shed more light on the influence of correlations, which, of course, would come at much higher computational cost when taking into account all processes that are considered in the present work.

For future studies, it would also be interesting to combine our method with band structures and matrix elements obtained from density functional theory calculations (e.g., Refs. [56] and [57]) in order to obtain material-specific results. It is known from the study of silicon and diamond that the electron and phonon band structure of semiconductors and dielectrics can change significantly during drastic excitations [34,58,59] and it would be interesting to develop models to capture the interplay of band structure changes and the dynamics of nonthermalized electron and phonon distributions in the future.

ACKNOWLEDGMENTS

The authors would like to gratefully acknowledge funding by the Deutsche Forschungsgemeinschaft via Grant No. RE1141/15 as well as computation time on the Elwetritsch high-performance computing cluster granted by the AHRP under Project Lainel.

[1] M. Aeschlimann, M. Bauer, S. Pawlik, W. Weber, R. Burgermeister, D. Oberli, and H. C. Siegmann, Phys. Rev. Lett. **79**, 5158 (1997).

[2] O. Schmidt, M. Bauer, C. Wiemann, R. Porath, M. Scharte, O. Andreyev, G. Schönhense, and M. Aeschlimann, Appl. Phys. B **74**, 223 (2002).

[3] S. Mathias, A. Ruffing, F. Deicke, M. Wiesenmayer, M. Aeschlimann, and M. Bauer, Phys. Rev. B **81**, 155429 (2010).

[4] E. Turgut, C. La-o-vorakiat, J. M. Shaw, P. Grychtol, H. T. Nembach, D. Rudolf, R. Adam, M. Aeschlimann, C. M. Schneider, T. J. Silva, M. M. Murnane, H. C. Kapteyn, and S. Mathias, Phys. Rev. Lett. **110**, 197201 (2013).

[5] A. Sommer, E. M. Bothschafter, S. A. Sato, C. Jakubeit, T. Latka, O. Razskazovskaya, H. Fattahi, M. Jobst, W. Schweinberger, V. Shirvanyan, V. S. Yakovlev, R. Kienberger, K. Yabana, N. Karpowicz, M. Schultze, and F. Krausz, Nature (London) **534**, 86 (2016).

[6] K. Sokolowski-Tinten, C. Blome, J. Blums, A. Cavalleri, C. Dietrich, A. Tarasevitch, I. Uschmann, E. Förster, M. Kammler, M. Horn-von Hoegen, and D. von der Linde, Nature (London) **422**, 287 (2003).

[7] A. M. Lindenberg, J. Larsson, K. Sokolowski-Tinten, K. J. Gaffney, C. Blome, O. Synnergren, J. Sheppard, C. Caleman, A. G. MacPhee, D. Weinstein *et al.*, Science **308**, 392 (2005).

[8] A. Barty, S. Boutet, M. J. Bogan, S. Hau-Riege, S. Marchesini, K. Sokolowski-Tinten, N. Stojanovic, R. Tobey, H. Ehrke, A. Cavalleri, S. Düsterer, M. Frank, S. Bajt, B. W. Woods, M. M. Seibert, J. Hajdu, R. Treusch, and H. N. Chapman, Nat. Photon. **2**, 578 (2008).

[9] T. Rohwer, S. Hellmann, M. Wiesenmayer, C. Sohrt, A. Stange, B. Slomski, A. Carr, S. Mathias, L. Kipp, K. Rossnagel, M. Bauer, Y. Liu, L. M. Avila, and M. Kalla, Nature (London) **471**, 490 (2011).

[10] A. Vogel and V. Venugopalan, Chem. Rev. **103**, 577 (2003).

[11] B. N. Chichkov, C. Momma, S. Nolte, F. von Alvensleben, and A. Tünnermann, Appl. Phys. A **63**, 109 (1996).

[12] T. E. Cowan, J. Fuchs, H. Ruhl, A. Kemp, P. Audebert, M. Roth, R. Stephens, I. Barton, A. Blazevic, E. Brambrink *et al.*, Phys. Rev. Lett. **92**, 204801 (2004).

[13] R. R. Gattass and E. Mazur, Nat. Photon. **2**, 219 (2008).

[14] D. Bäuerle, *Laser Processing and Chemistry* (Springer-Verlag, Berlin, 2011).

[15] P. Balling and J. Schou, Rep. Prog. Phys. **76**, 036502 (2013).

[16] I. Mirza, N. M. Bulgakova, J. Tomáštík, V. Michálek, O. Haderka, L. Fekete, and T. Mocek, Sci. Rep. **6**, 39133 (2016).

[17] M. V. Shugaev, C. Wu, O. Armbruster, A. Naghilou, N. Brouwer, D. S. Ivanov, T. J.-Y. Derrien, N. M. Bulgakova, W. Kautek, B. Rethfeld, and L. V. Zhigilei, MRS Bull. **41**, 960 (2016).

[18] F. Dorchies and V. Recoules, Phys. Rep. **657**, 1 (2016).

[19] B. C. Stuart, M. D. Feit, S. Herman, A. M. Rubenchik, B. W. Shore, and M. D. Perry, Phys. Rev. B **53**, 1749 (1996).

[20] A. C. Tien, S. Backus, H. Kapteyn, M. Murnane, and G. Mourou, Phys. Rev. Lett. **82**, 3883 (1999).

[21] M. Lenzner, J. Krüger, S. Sartania, Z. Cheng, C. Spielmann, G. Mourou, W. Kautek, and F. Krausz, Phys. Rev. Lett. **80**, 4076 (1998).

[22] L. V. Keldysh, Zh. Eksp. Teor. Fiz. **47**, 1945 (1964) [Sov. Phys. JETP **20**, 1307 (1965)].

[23] L. V. Keldysh, Zh. Eksp. Teor. Fiz. **37**, 713 (1959) [Sov. Phys. JETP **10**, 509 (1960)].

[24] N. Bloembergen, IEEE J. Quantum Electron. **10**, 375 (1974).

[25] B. C. Stuart, M. D. Feit, A. M. Rubenchik, B. W. Shore, and M. D. Perry, Phys. Rev. Lett. **74**, 2248 (1995).

[26] F. Quéré, S. Guizard, and P. Martin, Europhys. Lett. **56**, 138 (2001).

[27] V. V. Temnov, K. Sokolowski-Tinten, P. Zhou, A. El-Khamhawy, and D. von der Linde, Phys. Rev. Lett. **97**, 237403 (2006).

[28] A. Mouskeftaras, S. Guizard, N. Fedorov, and S. Klimentov, Appl. Phys. A **110**, 709 (2013).

[29] B. Rethfeld, Phys. Rev. Lett. **92**, 187401 (2004).

[30] B. Rethfeld, Phys. Rev. B **73**, 035101 (2006).

[31] J. R. Gulley and T. E. Lanier, Phys. Rev. B **90**, 155119 (2014).

[32] A. Kaiser, B. Rethfeld, M. Vicanek, and G. Simon, Phys. Rev. B **61**, 11437 (2000).

[33] N. S. Shcheblanov and T. E. Itina, Appl. Phys. A **110**, 579 (2013).

[34] P. Stampfli and K. H. Bennemann, Phys. Rev. B **49**, 7299 (1994).

[35] H. M. van Driel, Phys. Rev. B **35**, 8166 (1987).

[36] A. Rämer, O. Osmani, and B. Rethfeld, J. Appl. Phys. **116**, 053508 (2014).

[37] K. Nakajima, T. Kitayama, H. Hayashi, M. Matsuda, M. Sataka, M. Tsujimoto, M. Toulemonde, S. Bouffard, and K. Kimura, Sci. Rep. **5**, 13363 (2015).

[38] S. I. Anisimov, B. L. Kapeliovich, and T. L. Perel'man, Sov. Phys. JETP **39**, 375 (1974).

[39] M. Lisowski, P. A. Loukakos, U. Bovensiepen, J. Stähler, C. Gahl, and M. Wolf, Appl. Phys. A **78**, 165 (2004).

[40] Z. Lin, L. V. Zhigilei, and V. Celli, Phys. Rev. B **77**, 075133 (2008).

[41] T. Gunst, T. Markussen, K. Stokbro, and M. Brandbyge, Phys. Rev. B **93**, 035414 (2016).

[42] B. Y. Mueller and B. Rethfeld, Phys. Rev. B **87**, 035139 (2013).

[43] B. Y. Mueller and B. Rethfeld, Appl. Surf. Sci. **302**, 24 (2014).

[44] B. Rethfeld, H. Krutsch, and D. H. H. Hoffmann, Contrib. Plasma Phys. **50**, 16 (2010).

[45] N. Brouwer and B. Rethfeld, J. Opt. Soc. Am. B **31**, C28 (2014).

[46] Gnu scientific library, http://www.gnu.org/software/gsl/.

[47] W. Porod and D. K. Ferry, Phys. Rev. Lett. **54**, 1189 (1985).

[48] D. Arnold, E. Cartier, and D. J. DiMaria, Phys. Rev. B **49**, 10278 (1994).

[49] D. A. Chapman and D. O. Gericke, Phys. Rev. Lett. **107**, 165004 (2011).

[50] N. Medvedev, U. Zastrau, E. Förster, D. O. Gericke, and B. Rethfeld, Phys. Rev. Lett. **107**, 165003 (2011).

[51] U. Zastrau, C. Fortmann, R. R. Fäustlin, L. F. Cao, T. Döppner, S. Düsterer, S. H. Glenzer, G. Gregori, T. Laarmann, H. J. Lee *et al.*, Phys. Rev. E **78**, 066406 (2008).

[52] L. Waldecker, R. Bertoni, R. Ernstorfer, and J. Vorberger, Phys. Rev. X **6**, 021003 (2016).

[53] H. Zhao and J. B. Freund, J. Appl. Phys. **104**, 033514 (2008).

[54] R. Binder, H. S. Köhler, M. Bonitz, and N. Kwong, Phys. Rev. B **55**, 5110 (1997).

[55] M. Bonitz, *Quantum Kinetic Theory* (Springer, Cham, Switzerland, 2016).

[56] B. Monserrat and R. J. Needs, Phys. Rev. B **89**, 214304 (2014).

[57] E. S. Zijlstra, F. Cheenicode Kabeer, B. Bauerhenne, T. Zier, N. Grigoryan, and M. E. Garcia, Appl. Phys. A **110**, 519 (2013).

[58] H. O. Jeschke and M. E. Garcia, in *Nonlinear Optics, Quantum Optics, and Ultrafast Phenomena with X-Rays*, edited by B. W. Adams (Springer, Boston, MA, 2003).

[59] I. Klett, T. Zier, B. Rethfeld, M. E. Garcia, and E. S. Zijlstra, Phys. Rev. B **91**, 144303 (2015).